



NUMERICAL STUDY OF g-JITTER INDUCED DOUBLE-DIFFUSIVE CONVECTION

Y. Shu and B. Q. Li

*Department of Mechanical Engineering, Washington State University,
 Pullman, Washington, USA*

H. C. de Groh

NASA Lewis Research Center, Cleveland, Ohio, USA

A finite element study is presented of double-diffusive convection driven by g-jitter in a microgravity environment. Mathematical formulations are presented and extensive simulations are carried out for g-jitter induced fluid flow, temperature distribution, and solutal transport in an alloy system under consideration for space flights. Computations include the use of idealized single-frequency and multifrequency g-jitter as well as the real g-jitter data taken during an actual Space Shuttle flight. Little correlation is seen between these velocity components for the g-jitter components studied. The temperature field is basically undisturbed by convection because of a small Pr number for the fluid. The disturbance of the concentration field, however, is pronounced, and the local variation of the concentration follows the velocity oscillation in time. It is found that although the concentration field varies in both position and time, the local concentration gradient remains approximately constant in time. Numerical study further indicates that with an increase in g-jitter force (or amplitude), the nonlinear convective effects become much more obvious, which in turn drastically change the concentration fields. The simulated results computed using the g-jitter data taken during space flights show that both the velocity and concentration become random, following approximately the same pattern as the g-jitter perturbations.

INTRODUCTION

Understanding the effect of gravity perturbation, or g-jitter, on thermally induced convection in microgravity is of critical importance in designing and optimizing thermal fluids systems for space materials processing. Alloy solidification experiments conducted in space vehicles showed that the solute uniformity and defects formation in space grown crystals are strongly affected by natural convection in the melt pool that arises as a result of the combined action of temperature and concentration gradients in the melt and gravity [1-4]. These deleterious effects

Received 29 February 2000; accepted 6 October 2000.

The authors gratefully acknowledge the support of this work by NASA (Grant No. NCC8-92 and NAG8-1693).

Address correspondence to Professor Ben Q. Li, School of Mechanical and Materials Engineering, Washington State University, P.O. Box 642920, Pullman, WA 99164, USA. E-mail: li@mme.wsu.edu

NOMENCLATURE

C_p	heat capacity	u	dimensionless velocity
C_H, C_L	maximum and minimum concentration	u, v	x and y component of the dimensionless velocity
ΔC	concentration difference	V	volume of the cavity
C_0	dimensionless concentration	x, y	dimensionless coordinates
D	solutal diffusivity	α	thermal diffusivity
e	unit vector	β_C	solutal expansion coefficient
f	dimensionless frequency of the acceleration	β_T	thermal expansion coefficient
f^*	frequency of the acceleration	ϕ	shape function for velocity
g	dimensionless amplitude of the acceleration	θ	shape function for temperature and concentration
g^*	amplitude of the acceleration	ψ	shape function for pressure
g_0	earth gravity	μ	dynamic viscosity
Gr_s	solutal Grashof number, $Gr_T = g\beta_T \Delta CL^3/v^2$	ν	kinematic viscosity
Gr_T	thermal Grashof number, $Gr_S = g\beta_C \Delta TL^3/v^2$	$\partial\Omega$	boundary of computational domain
\hat{i}, \hat{j}	unit vectors of the i th, j th components	∇	gradient operator
k	thermal conductivity	ρ	density
L	length of the square cavity	Ω	computational domain
P	discretized nodal pressure array		
Pr	Prandtl number, $Pr = \nu/\alpha$		
Sc	Schmidt number, $Sc = \nu/D$		
T	dimensionless temperature		
T_H, T_L	maximum and minimum temperatures		
ΔT	temperature between T_H and T_L		
			Subscripts
		i, j	i th, j th point
		n	n th component
			Superscripts
		i, j	i th, j th component
		T	matrix transpose

generally are considered to be a culprit for the nonrepeatability of the quality of crystals grown in microgravity [5-8].

Gravity perturbation or g-jitter originates from a variety of sources including crew motions, mechanical vibrations (pumps, motors, excitations of natural frequencies of spacecraft structures), spacecraft maneuvers and attitude, atmosphere drag, and the Earth's gravity gradient [9]. Figure 1 shows the typical signature of g-jitter registered by an accelerometer installed on the Space Shuttle during an actual space flight. Clearly, g-jitter is random in both time and direction and is sharply different from terrestrial environment. Research on g-jitter induced natural convection in single component fluid flow systems suggests that convection in microgravity is related to the magnitude and frequency of g-jitter and to the alignment of the gravity field with respect to the direction of the temperature gradient in melt processing systems [5, 6]. Recently, both 2-D and 3-D numerical simulations have been conducted to estimate and calculate the adverse effects of time varying g-jitter [5, 6, 10-13]. The calculations used both idealized single- and multiple-frequency g-jitter modulations. These studies showed that the frequency, amplitude, and spatial orientation of the residual gravity vector all play an important role in

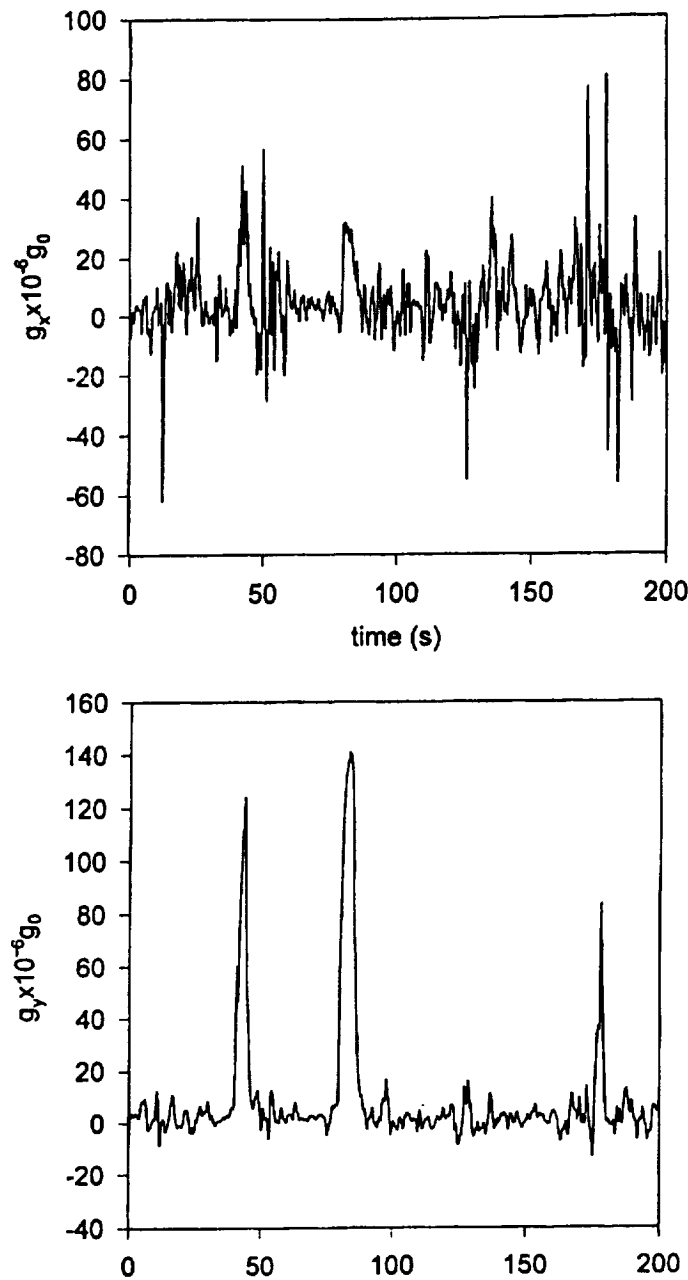


Figure 1. Signature of g-jitter data in the x - and y -directions as a function of time registered by an accelerometer aboard the Space Shuttle. Time is measured in seconds.

determining the convective flow behavior of a melt being processed in space. When the residual accelerations oscillate about the positive and negative of an axis, the orientation of this direction relative to the density gradient determines whether a mean flow is generated in the liquid [5, 6]. Sinusoidal oscillating accelerations induce an oscillating convective flow in the liquid. The resultant velocity fields oscillate with the same frequency as the affecting gravity field.

Although these studies are useful in illustrating the basic features of g-jitter induced convection in a single component system, very little information seems to be available on the fundamental understanding of double-diffusive convection in a microgravity environment. An exception is a paper published in a recent conference proceedings by Bune et al. [14], who discussed double-diffusive convection during solidification of HgCdTe. The study of double-diffusive convection can be of critical importance in binary alloy solidification systems, because the quality of the final products is strongly correlated to the concentration distribution in the melt during processing. The main reason for conducting solidification experiments in space is to eliminate convection induced solutal striation. Several alloy solidification experiments are currently being planned for future Space Shuttle flights and for the International Space Station under construction. This paper presents a numerical analysis of double-diffusive convection induced by g-jitter in one of these alloys melt systems in microgravity environment. Toward this end, a simple 2-D cavity geometry is considered and the Navier-Stokes equations, energy equations and solutal transport equations are solved using the finite element method. The analyses will be presented of the effects of both the g-jitter data synthesized using the Fourier series transformation as well as real g-jitter data taken directly during space flights. The information and computation methodology should be of great value for gaining an understanding of the basic physics governing the g-jitter induced double-diffusive convection, which allows rational guidelines to be developed for designing and operating thermal fluids systems for space experiments involving binary melt processing.

PROBLEM STATEMENT

Figure 2 schematically illustrates the model problem to be studied along with the coordinate system for analysis. We consider a square cavity filled with a binary liquid metal alloy. Its left side is fixed at a higher concentration C_H and right side at a higher temperature T_H . One of the important characteristics is that the solutal Grashof number Gr_S and the thermal Grashof number $[Gr_T]$ be approximately the same. The dimension of the square is set to L , as nondimensionalized, equal to 1. The upper and lower walls are kept adiabatic. The origin of the coordinate system is selected at the lower left corner of the cavity. In microgravity, double-diffusive melt convection arises because of the combined effect of the temperature and concentration gradients and the time varying gravity perturbation. The melt flow in turn will alter, in principle, both the thermal and concentration fields. The objective of this paper is to develop a basic understanding of g-jitter double-diffusive convection and its effect on solutal distribution in the melt mixture, through extensive numerical simulations and analyses.

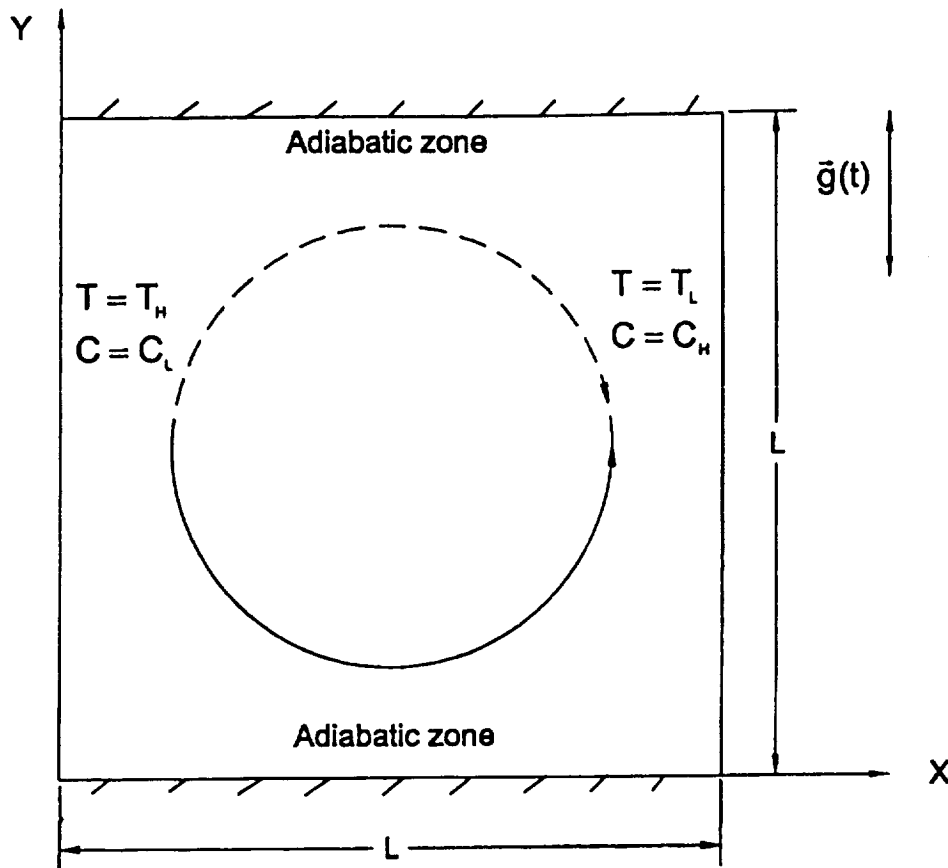


Figure 2. Schematic representation of g-jitter driven oscillating convection in a 2-D cavity in microgravity environment.

While g-jitter in general is random in both time and direction, as seen in Figure 1, in some cases and for a certain period of time, g-jitter may be partially represented by a synthesized Fourier series via the fast Fourier transformation, viz.,

$$g^*(t^*) = \sum_{n=1}^N g_n^* \sin(2\pi f_n^* t^*) e \quad (1)$$

where g_n^* and f_n^* are the amplitude and frequency of the n th acceleration component, respectively. Here the subscript * designates a dimensional quality.

The g-jitter induced melt flow, heat, and mass transport in the system are governed by the continuity equation, the Navier-Stokes equations, the energy balance equation, and the species conservation equation. For the current system, these equations are written in a nondimensionalized form as follows:

$$\nabla \cdot \mathbf{u} = 0 \quad (2)$$

$$\frac{\partial \mathbf{u}}{\partial t} + (\mathbf{u} \cdot \nabla) \mathbf{u} = -\nabla P + \nabla^2 \mathbf{u} - (\text{Gr}_T T + \text{Gr}_S C) \mathbf{g}(t) \quad (3)$$

$$\frac{\partial T}{\partial t} + \mathbf{u} \cdot \nabla T = \frac{1}{\text{Pr}} \nabla^2 T \quad (4)$$

$$\frac{\partial C}{\partial t} + \mathbf{u} \cdot \nabla C = \frac{1}{\text{Sc}} \nabla^2 C \quad (5)$$

In the above equations, lengths are nondimensionalized by L , velocity by v/L , time by L^2/v , temperature by $\Delta T = T_H - T_L$, and concentration by $\Delta C = C_H - C_L$. Also use has been made of Boussinesq's approximation, $\rho(T, C) = \rho_0(1 - \beta_T(T - T_0) - \beta_C(C - C_0))$, and $\mathbf{g}(t)$ is nondimensionalized by $g_0 = 9.8 \text{ m/s}^2$.

To obtain solutions to the above equations, the following boundary conditions are applied:

$$\mathbf{u} = 0 \text{ at } x = 0 \text{ and } x = 1 \text{ and } y = 0 \text{ and } y = 1$$

$$\frac{\partial T}{\partial y} = \frac{\partial C}{\partial y} = 0 \text{ at } y = 0 \text{ and } y = 1$$

$$T = 1 \quad C = 0 \quad \text{at } x = 0$$

$$T = 0 \quad C = 1 \quad \text{at } x = 1$$

THE FINITE ELEMENT SOLUTION

The above governing equations along with the boundary conditions are solved using the standard Galerkin finite element method. The stiffness matrix is obtained by using Galerkin's method of weighted residuals. Following the procedures given in [15, 16], the governing equations are recast in the following integral forms

$$\left(\int_{\Omega} \hat{\psi}^j \cdot \nabla \phi^T dV \right) \mathbf{U}_j = -\varepsilon \left(\int_{\Omega} \psi \psi^T dV \right) \mathbf{P} \quad (6)$$

$$\begin{aligned} & \left(\int_{\Omega} \phi \phi^T dV \right) \frac{d\mathbf{U}_i}{dt} + \left(\int_{\Omega} \phi \mathbf{u} \cdot \nabla \phi^T dV \right) - \left(\int_{\Omega} \hat{i} \cdot \nabla \phi \psi^T dV \right) \mathbf{P} \\ & + \left(\int_{\Omega} \nabla \phi \cdot \nabla \phi^T dV \right) \mathbf{U}_i + \left(\int_{\Omega} (\hat{i} \cdot \nabla \phi) (\hat{j} \cdot \nabla \phi^T) dV \right) \mathbf{U}_j \\ & + \left(\int_{\Omega} \text{Gr}_T g_i \phi \theta^T \right) \mathbf{T} + \left(\int_{\Omega} \text{Gr}_S g_i \phi \theta^T \right) \mathbf{C} = \int_{\partial\Omega} \mathbf{n} \cdot \boldsymbol{\tau} \cdot \hat{i} \phi dS \end{aligned} \quad (7)$$

$$\left(\int_{\Omega} \theta \theta^T dV \right) \frac{dT}{dt} + \left(\int_{\Omega} \theta \mathbf{u} \cdot \nabla \theta^T dV \right) T + \left(\int_{\Omega} \frac{1}{Pr} \nabla \theta \cdot \nabla \theta^T dV \right) T = - \int_{\partial\Omega} q_T \theta dS \quad (8)$$

$$\left(\int_{\Omega} \theta \theta^T dV \right) \frac{dC}{dt} + \left(\int_{\Omega} \theta \mathbf{u} \cdot \nabla \theta^T dV \right) C + \left(\int_{\Omega} \frac{1}{Sc} \nabla \theta \cdot \nabla \theta^T dV \right) C = - \int_{\partial\Omega} q_T \theta dS \quad (9)$$

Once the forms of shape functions ϕ , θ , and ψ are specified, the integrals defined in the above equations can be calculated numerically over each individual element. Combining the discretized momentum, energy, and solutal transport equations gives rise to the following global finite element stiffness matrix equation:

$$\begin{bmatrix} \mathbf{M} & 0 & 0 \\ 0 & \mathbf{N}_T & 0 \\ 0 & 0 & \mathbf{N}_C \end{bmatrix} \begin{bmatrix} \dot{\mathbf{U}} \\ \dot{\mathbf{T}} \\ \dot{\mathbf{C}} \end{bmatrix} + \begin{bmatrix} \mathbf{A}(\mathbf{U}) + \mathbf{K} + 1/\varepsilon \mathbf{EM}_p^{-1} \mathbf{E}^T & \mathbf{B}_T & \mathbf{B}_C \\ 0 & \mathbf{D}_T(\mathbf{U}) + \mathbf{L}_T & 0 \\ 0 & 0 & \mathbf{D}_C(\mathbf{U}) + \mathbf{L}_C \end{bmatrix} \begin{bmatrix} \mathbf{U} \\ \mathbf{T} \\ \mathbf{C} \end{bmatrix} = \begin{bmatrix} \mathbf{F} \\ \mathbf{G}_T \\ \mathbf{G}_C \end{bmatrix} \quad (14)$$

It is noted that in constructing the above element matrix equation, the penalty formulation has been applied, and \mathbf{P} in the momentum equation is substituted by $(1/\varepsilon)\mathbf{M}_p^{-1} \mathbf{E}^T \mathbf{U}$. The assembled global matrix equations are stored in the skyline form and solved using the Gaussian elimination method. The above coefficient matrices from above are calculated by

$$\begin{aligned} \mathbf{M}_p &= \int_{\Omega} \psi \psi^T dV & \mathbf{N}_T &= \int_{\Omega} \theta \theta^T dV \\ \mathbf{M} &= \int_{\Omega} \phi \phi^T dV & \mathbf{N}_C &= \int_{\Omega} \theta \theta^T dV \\ \mathbf{E}_j &= \int_{\Omega} \hat{\mathbf{j}} \cdot \nabla \phi \psi^T dV & \mathbf{L}_C &= \int_{\Omega} \frac{1}{Sc} \nabla \theta \cdot \nabla \theta^T dV \\ \mathbf{L}_T &= \int_{\Omega} \frac{1}{Pr} \nabla \theta \cdot \nabla \theta^T dV & \mathbf{A}(\mathbf{U}) &= \int_{\Omega} \phi \mathbf{u} \cdot \nabla \theta^T dV \\ \mathbf{D}_C(\mathbf{U}) &= \int_{\Omega} \theta \mathbf{u} \cdot \nabla \theta^T dV & \mathbf{D}_T(\mathbf{U}) &= \int_{\Omega} \theta \mathbf{u} \cdot \nabla \theta^T dV \end{aligned}$$

$$\begin{aligned}
 \mathbf{B}_T &= \int_{\Omega} \mathbf{G} \mathbf{r}_T \mathbf{g} \theta^T dV & \mathbf{B}_C &= \int_{\Omega} \mathbf{G} \mathbf{r}_S \mathbf{g} \theta^T dV \\
 \mathbf{G}_T &= - \int_{\partial\Omega} q_T \theta dS & \mathbf{G}_C &= - \int_{\partial\Omega} q_C \theta dS \\
 \mathbf{F}_i &= \int_{\partial\Omega} \mathbf{n} \cdot \boldsymbol{\tau} \cdot \hat{\mathbf{i}} \phi dS \\
 \mathbf{K}_{ij} &= \left(\int_{\Omega} \nabla \phi \cdot \nabla \phi^T dV \right) \delta_{ii} + \int_{\Omega} (\hat{\mathbf{i}} \cdot \nabla \phi) (\hat{\mathbf{j}} \cdot \nabla \phi^T) dV
 \end{aligned}$$

RESULTS AND DISCUSSION

The transient finite element computational methodology described above enables the prediction of the transient convective flows driven by g-jitter, the temperature distribution and the solutal redistribution in the melt. The calculations were performed using a finite element code developed by our research group [16]. The code employs the backward Euler (or implicit) time difference scheme, with automatic time step control. The computer code was checked against other available commercial codes for fluid flow and thermal calculations, including FIDAP and FLUENT, and analytical solutions for a wide range of flows and thermal problems. Extensive numerical simulations were made. A selection of computed results is presented below and the parameters used for calculations are given in Table 1. Most transient calculations are started with an initial thermal and fluid flow field obtained with a constant gravity field of $g = 1 \times 10^{-6} g_0$ acting in the direction perpendicular to the growth direction to simulate a situation in which a long steady state microgravity is perturbed by g-jitter.

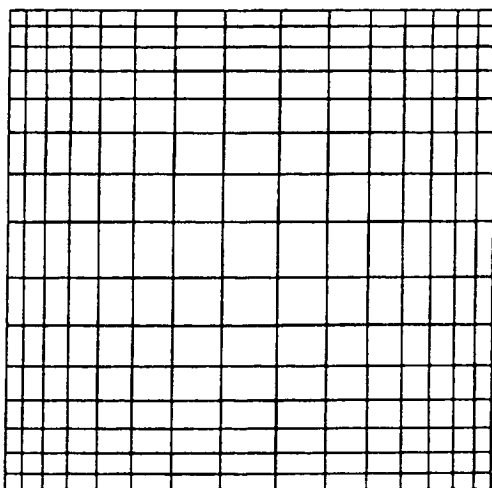
Prior to embarking upon numerical simulations, a variety of element types and nodal distributions were tested to obtain an appropriate mesh arrangement for computational accuracy and optimal computing time. The tests included 100, 225, 400, and 625 elements with 9 nodes and 400, 900, 1,600, and 2,500 4-node elements. For all these cases tested, a spatial distribution of nodes is arranged such that the spacing is reduced following the arithmetic progression from the middle of the cavity toward the four walls. The conditions used for the testing correspond to the maximum possible driving force for double-diffusive convection to be studied in this paper. These tests showed that 225 9-node elements with a node spacing decreased from the center toward the walls following an arithmetic progressive ratio of 0.3 that gave an optimal finite element mesh for the computation in both time and accuracy. Any further refinement of the mesh produces the results with an error less than 0.2%. The mesh is shown in Figure 3 and is used for all computations presented below.

During space flights, the idealized microgravity level is on the order of $1 \times 10^{-6} g_0$ and is essentially steady until a disturbance or g-jitter sets in. Thus, the transport variable fields may be considered to be in a quasisteady state when flights are in perfect condition, thereby enjoying the true benefit of microgravity. Figure 4 depicts the quasi steady state temperature, concentration, and fluid flow fields in the system under consideration for a typical steady microgravity condition.

Table 1. Parameters used in calculations

Dimensionless parameter	Value
Prandtl number (Pr)	0.012
Grashof number (Gr_T)	1.54E6
Grashof number (Gr_S)	-1.54E6
Schmidt number (Sc)	65.6

Apparently, the convection in the melt is very small, as indicated by the velocity plot, and so is the convective transport of energy and species in the system. The velocity arises near the hot wall and recirculates downward along the cold wall, forming a rotating flow loop. The transport of energy clearly is controlled by a diffusion mechanism, which is expected because of the small Prandtl number of the fluid. The convection, however, affects the concentration distribution in this case, as is evidenced by the distorted isosolutal contour lines. When the system is perturbed and g-jitter sets in, the ideal dynamic weightlessness condition is destroyed, and the microgravity level is no longer stable (see Figure 1) and changes both spatially and temporally, thereby inducing time dependent convective flows and the solutal striation. In some cases g-jitter can be represented by a synthesized Fourier series, which helps to facilitate simulations and analyses. In what is considered below, we present the analyses of the effects on the convection in the double-diffusive system that are generated by g-jitter with single-frequency and multifrequency, and by measured g-jitter data.

**Figure 3.** Finite element mesh for computation. Nine nodes are used in each element.

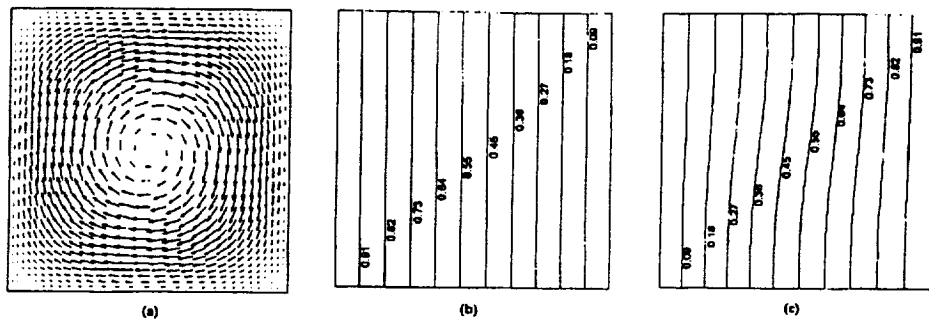


Figure 4. The steady state fluid flow field and its thermal and solute distribution caused by a constant g-jitter ($g = 10^{-6}g_0$) acting in the y -direction: (a) the velocity profile ($U_{\max} = 0.01211$); (b) the isothermal profile; and (c) the isoconcentration profile.

Single-Frequency g-Jitter

Single-frequency g-jitter represents a somewhat idealized situation in that the true g-jitter disturbance consists of a wide range of the frequency spectrum. However, a study of this idealized single-frequency disturbance helps us to gain a fundamental insight into the basic behavior of the double-diffusive convection. Space experiments suggested that melt growth systems are prone to the disturbance of the g-jitter components of low frequency. The harmful frequency range lies in the range of 0.001 to 1 Hz [5, 6]. Numerical results were obtained for g-jitter induced convection and are shown in Figures 5 and 6 for a g-jitter component of $g = 1 \times 10^{-3}g_0 \sin(0.2\pi t)$, which represents a typical harmful disturbance to a melt processing system, with the initial condition given in Figure 4. In Figure 5, the snapshots of the oscillating velocity and concentration profiles are given for one cycle period while the transient development of field variables is plotted at some specific locations in the cavity. As stated above, the temperature profile remains approximately the same with very little, unnoticeable oscillation and hence is omitted here. Inspection of these results shows that convective flow in the system has reached a quasisteady state in a time frame of approximately 3 or 4 periods, and afterwards it oscillates with basically the same frequency of the g-jitter (dimensionless period = 0.02688). The convection lags in phase, though, the phase angle being a function of the amplitude of the g-jitter component, the location, and flow field. That the flow oscillates with the same frequency of the driving g-jitter may be attributed to the fact that although the main flow is strong, the velocity gradient is much smaller, and thus the product of the two contributes negligibly to the flow.

The oscillating flow has a strong effect on concentration distribution. In fact, concentration, once it reached a quasisteady state, also oscillate harmonically with time with approximately the same frequency over a time-averaged value; again the phase angle is a function of the amplitude of the g-jitter component, the location, and flow field. For this system, it appears that the concentration oscillation primarily stems from the oscillating velocity field. There is yet no subharmonic (or

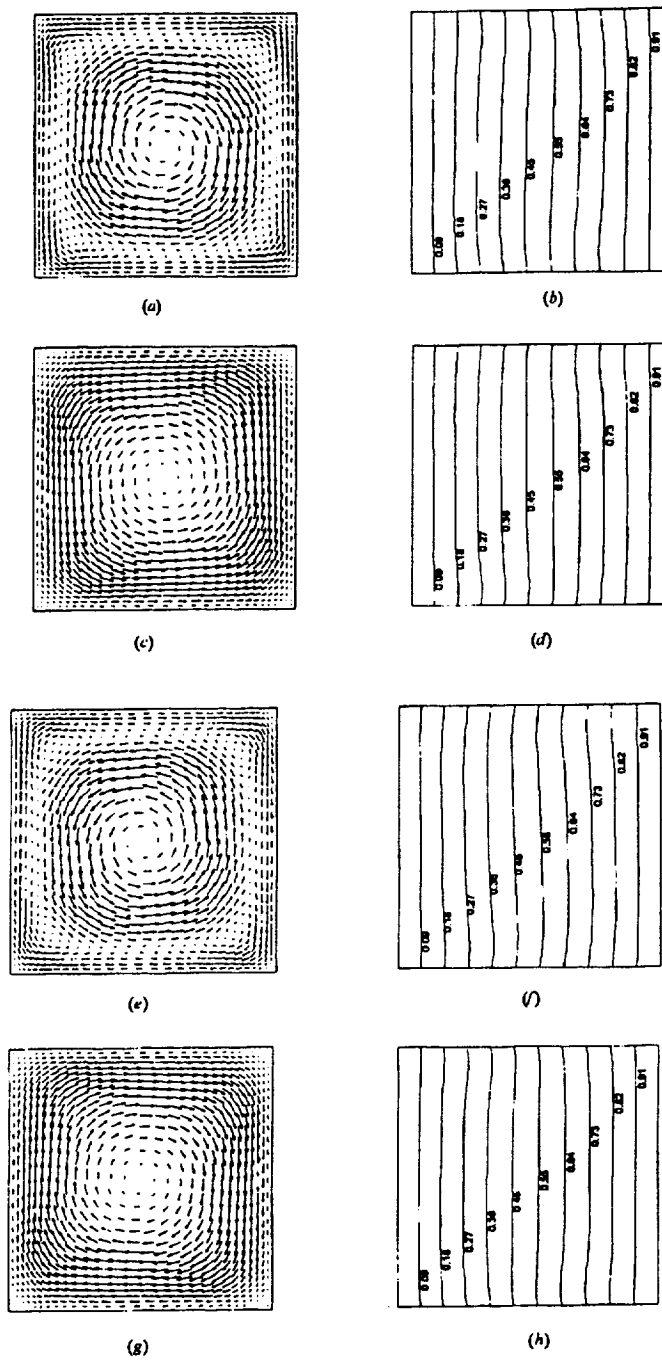


Figure 5. Evolution of the velocity (a)–(d) and concentration (e)–(h) fields induced by a single-frequency g-jitter driving force in the y -direction: (a) $t = 14.33163$ ($U_{\max} = 0.6367$); (b) $t = 14.33163$ concentration; (c) $t = 14.33970$ ($U_{\max} = 2.752$); (d) $t = 14.33970$ concentration; (e) $t = 14.34507$ ($U_{\max} = 0.6368$); (f) $t = 14.34507$ concentration; (g) $t = 14.35314$ ($U_{\max} = 2.752$); and (h) $t = 14.35314$ concentration.

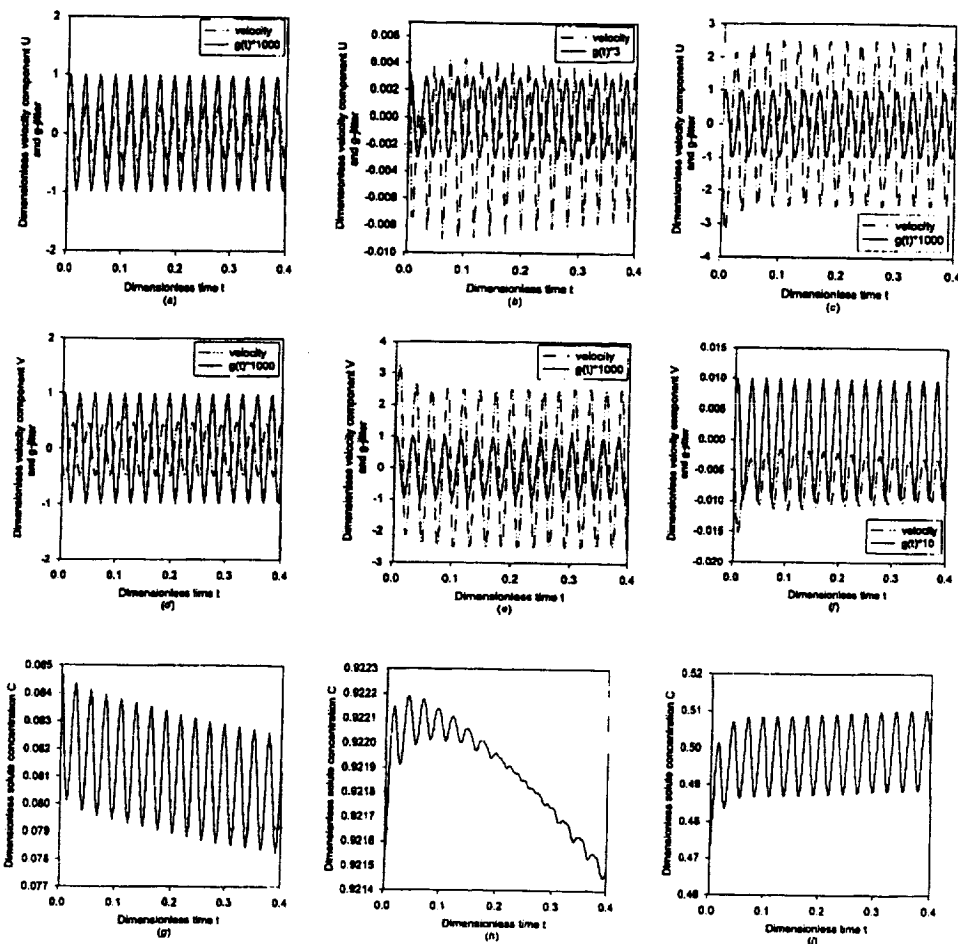


Figure 6. Time variation of velocity components U , V and concentration with oscillating gravity: (a), (d), (g) at $(0.07798, 0.07798)$; (b), (e), (h) at $(0.9220, 0.5)$; and (c), (f), (i) at $(0.5, 0.9220)$.

frequency-doubling) effect. In fact, detailed analyses show that although the concentration field oscillates in time, its gradient remains basically time independent. As a result, the product of the velocity and concentration gradient (or the initial term) follows the same frequency as the velocity, thereby producing the results as shown in Figure 6. This time harmonic oscillation is preceded by a transient period, which depends strongly on the location and direction of the concentration gradients (see Figure 6). For the points near the vertical wall where the main flow is perpendicular to the concentration gradients, the transient period is about 200 periods. For the points near the horizontal walls where convective flow is parallel to concentration gradients, the transient period is as long as 500 periods. The amplitude of concentration oscillation is also much larger at these locations, which clearly

is attributed to the fact that the flow parallel to the concentration gradient is much stronger.

Additional numerical simulations also were carried out by switching off either the concentration or temperature field. It is found that the combined double-diffusive convection for this particular system is approximately a superposition of the concentration and temperature fields, and that both thermal and solutal driving forces play almost equally important roles in driving the convection.

Extensive numerical experiments also were conducted for various g-jitter conditions and variations. Results suggest that the evolution and distribution of the field variables (velocity and concentration) are sensitive to the initial conditions. For example, if the initial fields are generated by a constant gravity field of $g_y = 10^{-3}g_0$, then the change in velocity will take much longer to reach a quasisteady state. For the same point near the middle bottom wall, it takes approximately 300 periods for the velocity to reach the time harmonic quasisteady state. For those points near the vertical walls, the transient period lasts about 700 cycles of oscillation.

Detailed analyses of the results indicate that there exists a subharmonic oscillation, or the doubling of frequency, in both secondary flow components (or velocity component perpendicular to the wall), although very weak. The concentration field, however, does not exhibit subharmonic oscillation until the amplitude of g-jitter is increased to $10^{-2}g_0$. Under this condition, the concentration contour is significantly distorted, and one of such cases is shown in Figure 7. The temperature field, however, remains the same until a much larger g-jitter amplitude, which is not at all realistic, is applied. The distorted concentration profile, combined with an increase in secondary flows, causes a more pronounced nonlinear oscillation (or frequency doubling) in velocity components perpendicular to the wall; the main flow components, however, remain basically the same in an oscillation pattern. Such a disturbed flow field causes the concentration distribution to be more strongly distorted. This is exhibited in both the concentration contour and the concentration oscillation at specific locations. As illustrated in Figure 8, the frequency-doubling effects, which clearly come from the convective term, start to show up in the velocity components perpendicular to the wall and in concentration as well after about 10 cycles of oscillation.

Multiple-Frequency g-Jitter

Let us now turn to the effects of multiple-frequency g-jitter on the convective behavior in the system. Toward this end, we select a representative frequency spectrum, $f = 10^{-3} \sim 1$ with $|g| = 10^{-4} \sim 10^{-1}g_0$, respectively, which are considered to be able to generate detrimental effects in melt processing systems. The computed results for velocity and concentration are plotted in Figures 9 and 10. As expected, the temperature field remains practically unchanged and hence is not shown. Detailed examination of the convection patterns shows that the main oscillating recirculating flow in the cavity is attributed to the g component with the largest amplitude and other components produce only perturbations that are superimposed on the main flows. This is further confirmed by the results of velocity

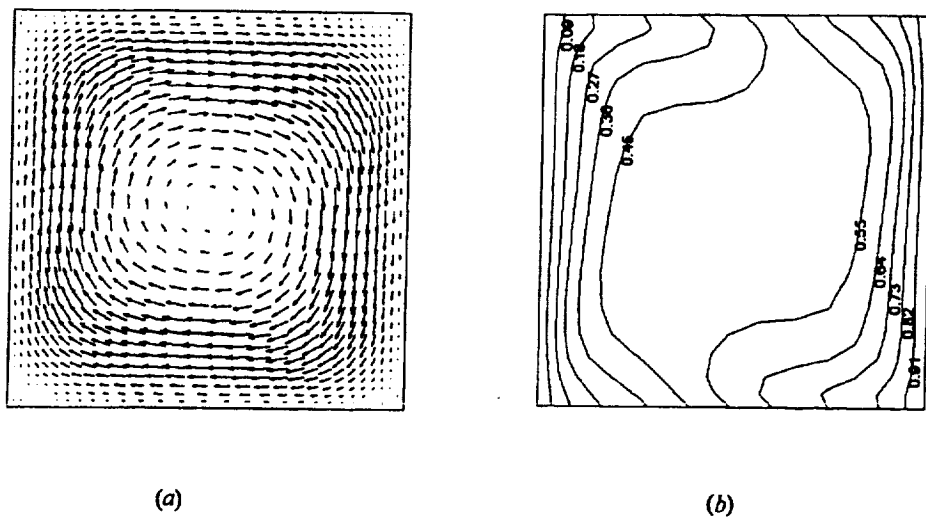


Figure 7. The dynamic development of the velocity and concentration fields generated by a single-frequency g-jitter driving force ($g = 10^{-2}g_0 \sin(0.2\pi t)$): (a) the velocity profile ($U_{\max} = 13.14$); (b) the isoconcentration profile.

and concentration variation at specific locations, from which it is clear that the evolution of the velocity and concentration fields is an approximate Fourier summation of velocities generated by each individual g-jitter component. This observation should not come as a surprise, in light of the above discussions on results obtained for single-frequency components.

Real g-Jitter Taken from Space Shuttle Flights

In reality, g-jitter is randomly in nature, as a result of a variety of sources can cause the perturbation of the dynamic weightlessness conditions of space vehicles in orbit. Numerical simulations were carried out using these real g-jitter data as shown in Figure 1 and some of the results are given in Figures 11 and 12. There exists no regulated transient pattern or time harmonic motion, and thus the convective flows in the system must be constantly monitored at any instant. The temperature field, however, remains the same, again a result of the predominance of thermal conduction in fluids. As might have been expected from the single and multiple g-jitter analyses, the flow pattern is similar with a single recirculating loop, but the time evolution is no longer regular in frequency because of the irregularity of the g-jitter driving force typical of the true nature of gravity perturbation in space. The time variation of velocities and concentration at specific locations further illustrates that the velocity responds quickly to the change in gravity perturbation, whereas the concentration does not. In fact, the concentration still is evolving in the transient stage, reflecting the mixed diffusive-convective nature of the concentration development in the system, even after the gravity perturbation disappears.

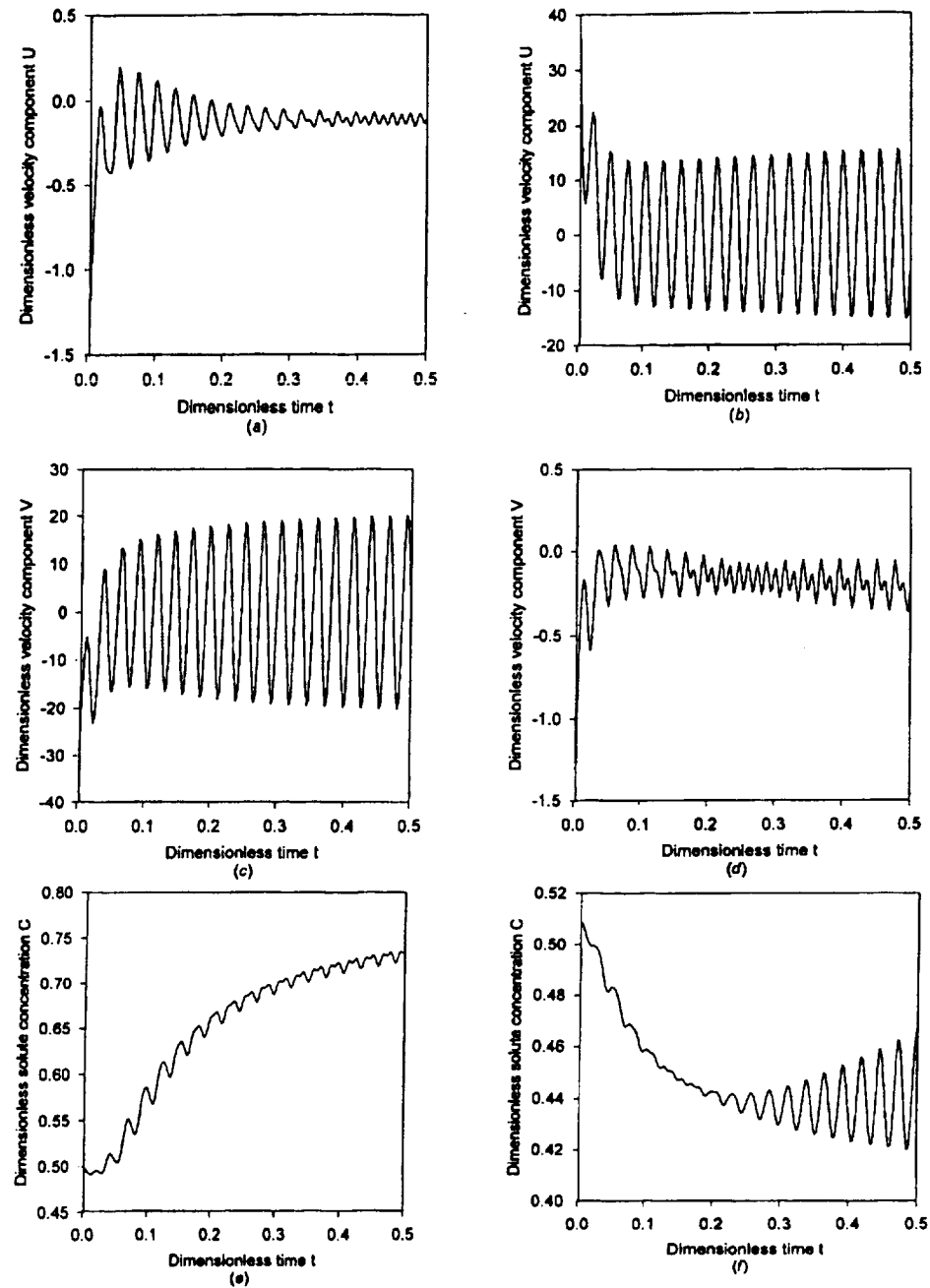


Figure 8. Time variation of velocity and concentration distribution with single-frequency g-jitter driving force ($g = 10^{-2}g_0 \sin(0.2\pi t)$): (a), (c), (e) velocity components U , V and concentration at (0.9220, 0.5); and (b), (d), (f) velocity components U , V and concentration at (0.5, 0.9220).

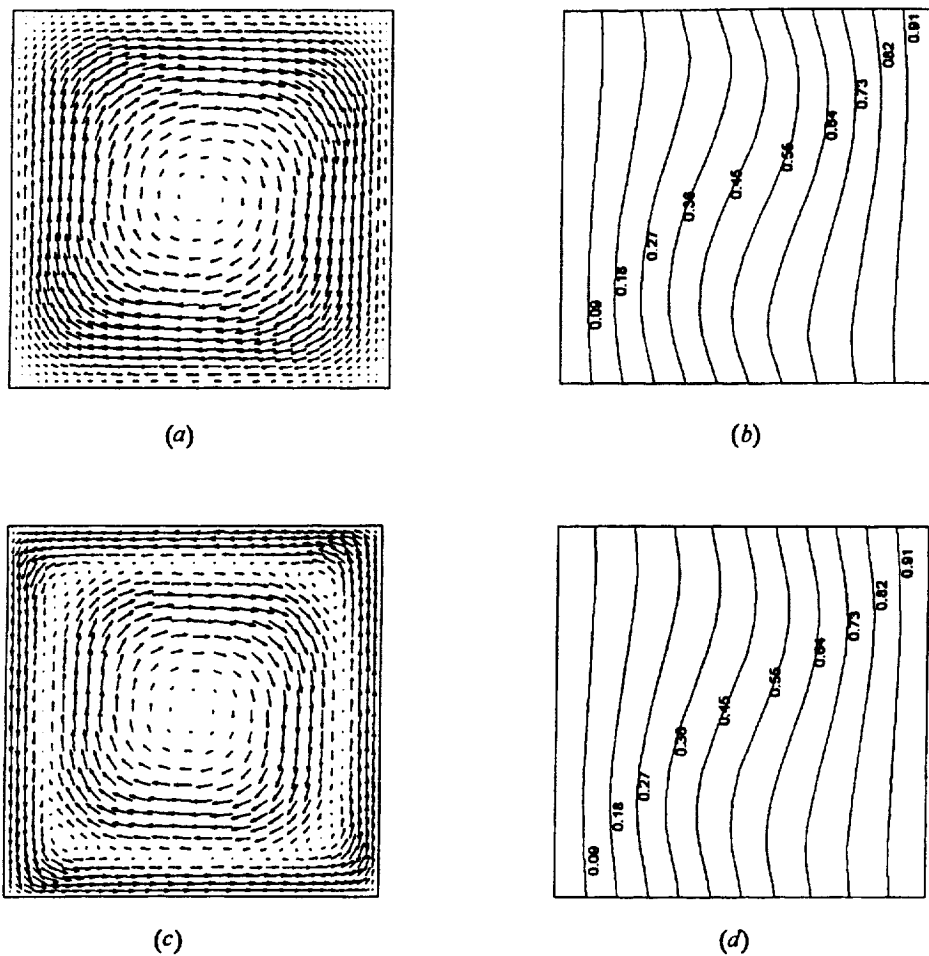


Figure 9. The dynamic development of the velocity and concentration fields caused by a multiple-frequency g-jitter driving force: (a) $t = 2.715245$ ($U_{\max} = 2.709$); (b) $t = 2.715245$ concentration profile; (c) $t = 2.745353$ ($U_{\max} = 0.5530$); and (d) $t = 2.745353$ concentration profile.

CONCLUDING REMAKRS

This paper has presented a finite element study of double diffusive convection driven by g-jitter in a microgravity environment. Extensive simulations were carried out using both the synthesized single- and multifrequency g-jitter and also the real g-jitter data taken during space flights. Results were analyzed for fluid flow, temperature distribution and solutal transport in an alloy system under consideration for Space Shuttle flights. Computed results suggest that for the system studied the main flow is in essence a combination of velocity components driven by each individual g-jitter component. The flow field is characterized by oscillating

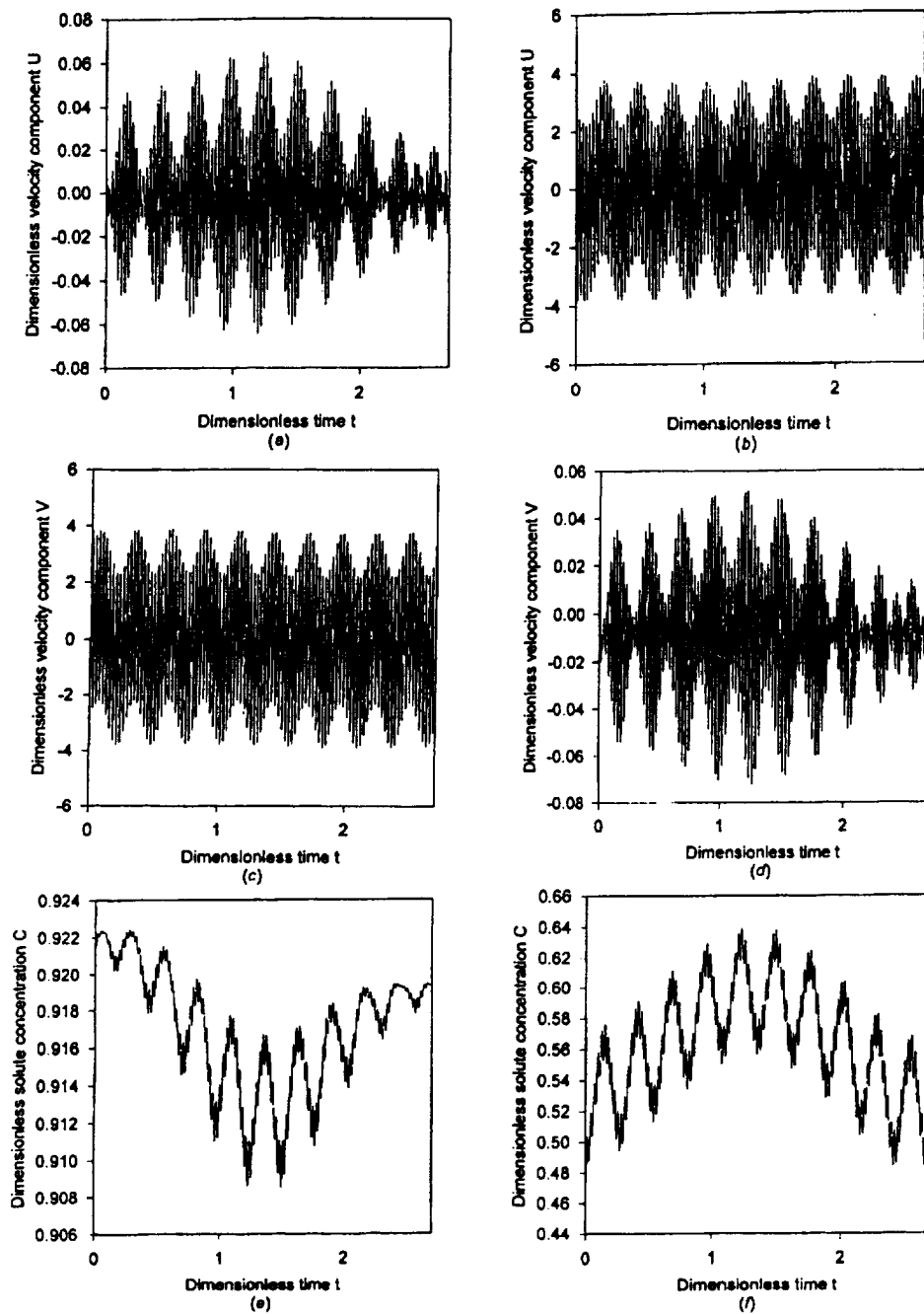


Figure 10. Time variation of velocity and concentration distribution caused by multiple frequency g-jitter driving force: (a, c, e) velocity components U , V and concentration at coordinate $(0.9220, 0.5)$, (b, d, f) velocity components U , V and concentration at coordinate $(0.5, 0.9220)$.

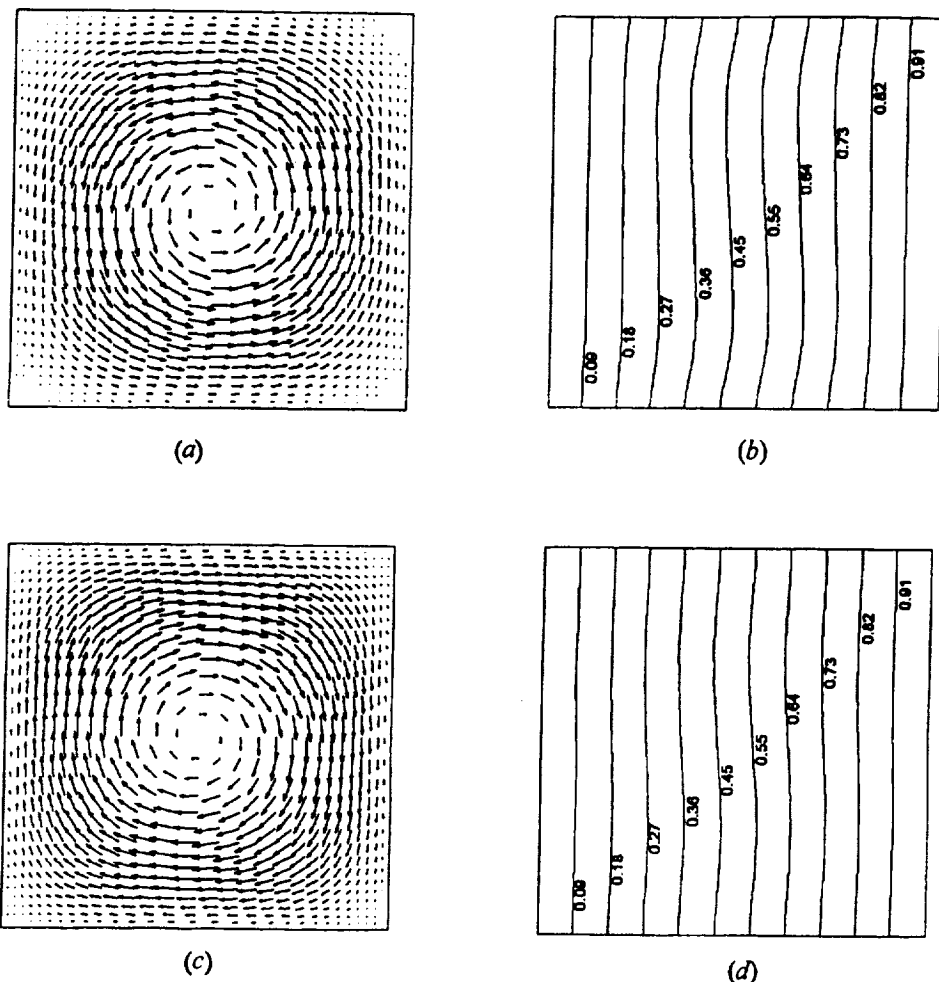


Figure 11. The dynamic development of the velocity and concentration fields caused by real g-jitter driving force: (a) $t = 0.2698170$ ($U_{\max} = 0.1579$); (b) $t = 0.2698170$ isoconcentration profile; (c) $t = 0.5386340$ ($U_{\max} = 0.06303$); and (d) $t = 0.5386340$ isoconcentration profile.

recirculating natural convection, with an oscillating frequency being equal to that of the driving g-jitter force. There exists a lag in the phase angle, which is a function of position, the local velocity, and the amplitude of the g-jitter force. There exists only a very short period of transient time, which lasts about a few periods of oscillation. The temperature field is basically undisturbed by convection because of the fact that the fluid has a small Pr number. The effect of convection on concentration distribution, however, is much more pronounced. The local variation of the concentration follows approximately the velocity oscillation in time. It is found that while the concentration varies in both position and time, the local concentration

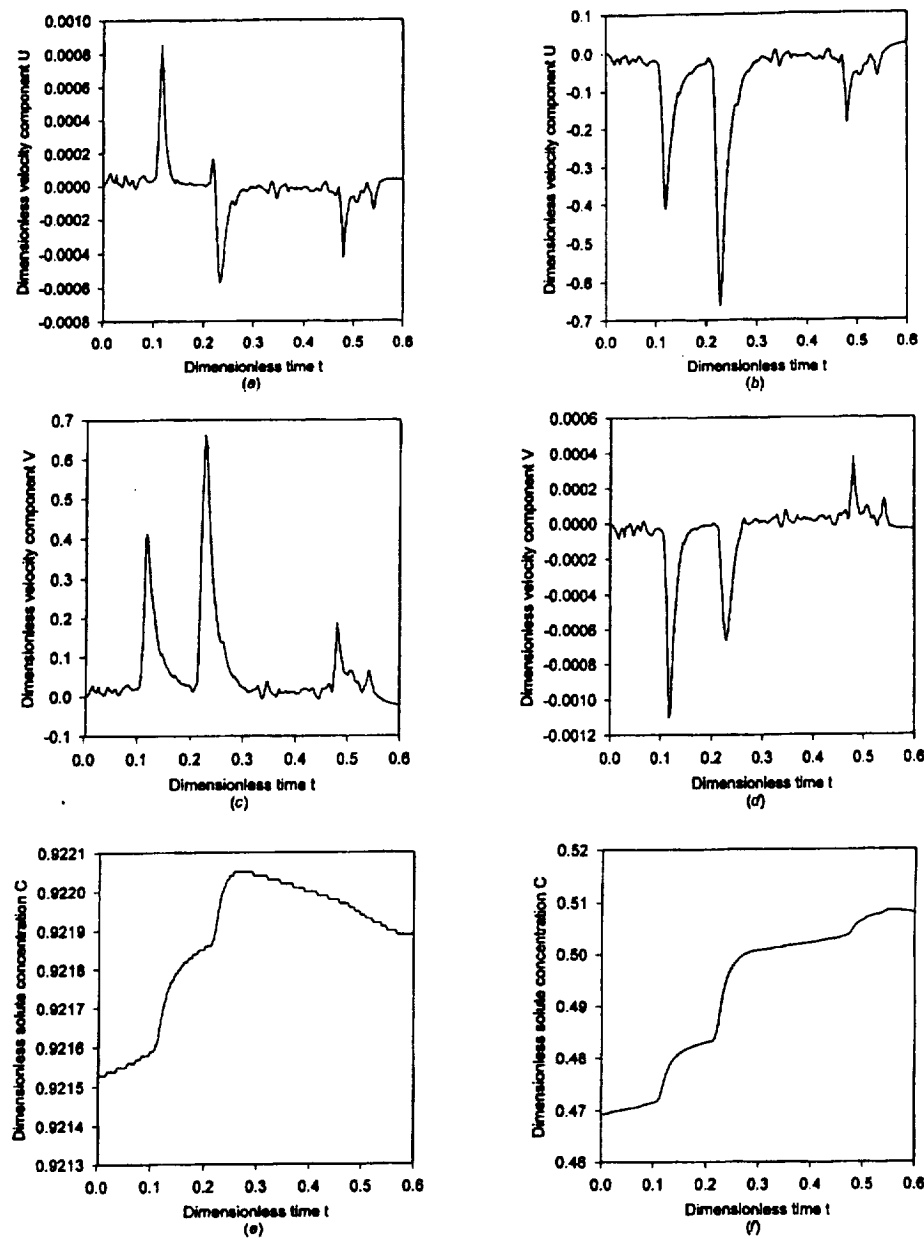


Figure 12. Time variation of velocity and concentration distribution under real g-jitter driving force: (a), (c), (e) velocity components U , V and concentration at $(0.9220, 0.5)$; (b), (d), (f) velocity components U , V and concentration at $(0.5, 0.9220)$.

gradient changes remain approximately constant in time. This is combined with the local velocity to give rise to the oscillating concentration field with the same frequency of flow field. The transient period for the concentration field is much longer than that for the velocity, however; and can be as long as 500 periods of oscillation before the concentration field finally reaches a quasisteady state time harmonic oscillation. Numerical results further indicate that with an increase in g-jitter force (or amplitude), the nonlinear convective effects become much more obvious, which in turn drastically change the concentration fields. The simulated results computed using the g-jitter data from real space flights show that both the velocity and concentration are random, following approximately the same pattern as the g-jitter.

REFERENCES

1. E. S. Nelson, *An Examination of Anticipated g-Jitter in Space Station and its Effects on Materials Processes*, NASA TM 103775, 1991.
2. H. C. de Groh, III, and E. S. Nelson, *On Residual Acceleration during Space Experiments*, ASME Winter Annual Meeting, Chicago, Nov 6-11, HTD vol 290, pp. 23-33, 1994.
3. S. Maruyama, T. Shibata, K. Tsukamoto, and K. Shimizu, Measurement of Solutal and Thermal Diffusion in Systems Subjected to Rapid Cooling under Microgravity during Parabolic Flight, *Heat Transfer—Japanese Research*, vol. 27, no. 2, pp. 114-129, 1998.
4. R. Monti and R. Savino, G-sensitivity of Microgravity Experimentation—Fundamental of Disturbance Response, *Microgravity Science and Technology*, vol. 11, no. 2, pp. 53-58, 1998.
5. J. I. D. Alexander, J. Ouazzani, and F. Rosenberger, Analysis of the Low Gravity Tolerance of Bridgman—Stockbarger Crystal Growth, I. Steady and Impulse Accelerations, *J. Crystal Growth*, vol. 97, pp. 21-28, 1989.
6. J. I. D. Alexander, S. Amirouidine, J. Ouazzani, and F. Rosenberger, Analysis of the Low Gravity Tolerance of Bridgman—Stockbarger Crystal Growth, II. Transient and Periodic Accelerations, *J. Crystal Growth*, vol. 113, pp. 21-38, 1991.
7. Y. Kamotani, L. Chao, S. Ostrach and H. Zhang, Effect of g-jitter on Free-Surface Motion in a Cavity, *J. Spacecraft and Rockets*, vol. 32, no. 1, pp. 177-183, 1995.
8. G. Neumann, Three-Dimensional Numerical Simulation of Buoyancy-Driven Convection in Vertical Cylinders Heated from Below, *J. Fluid Mechanics*, vol. 214, pp. 559-578, 1990.
9. B. N. Antar and V. S. Nuotio-Antar, *Fundamentals of Low Gravity Fluid Dynamics and Heat Transfer*, CRC Press, Boca Ration, FL, 1993.
10. H. Tang, Z. M. Tang, W.R. Hu, G. Chen, and B. Roux, Numerical Simulation of g-jitter Effect on Half Floating Zone Convection under Microgravity Environment, *Microgravity Science and Technology*, vol. 9, no. 1, pp. 28-34, 1996.
11. J. I. D. Alexander and R. M. Banish, Modeling G-Sensitivity of Low-Gravity Experiments, *Microgravity Science and Technology*, vol. 11, no 3, pp. 90-95, 1998.
12. M. J. B. Rogers and J. I. D. Alexander, Analysis of Spacelab 3 Residual Acceleration Data, *J. Spacecraft and Rockets*, vol. 28, no. 6, p. 707-712, 1991.
13. J. I. Ramos, G-Jitter Effect on Mass Transfer in Annular Liquid Jets, *Int. J. Numerical Methods for Heat and Fluid Flow*, vol. 6, no. 5, pp. 17-28, 1996.
14. A. V. Bune, D. C. Gillies, and S. L. Lehoczky, Effect of Gravity on the Double Diffusive Convection during Directional Solidification of a Non-Dilute Alloy with Application to HgCdTe, *Proc. of SPIE*, The International Society for Optical Engineering, vol. 3792, pp. 177-182, 1999.

15. O. C. Zienkiewicz and R. L. Taylor, *The Finite Element Method*, 4th ed., (Chap. 13) McGraw-Hill, New York, 1992.
16. S. P. Song and B. Q. Li, Surface Deformation and Marangoni Flow in Electrostatically Levitated Droplets, *Int. J. Heat Mass Transf.*, vol. 43, pp. 3589–3606, 2000.

